Continuous Control Set Predictive Speed Control of SPMSM Drives With Short Prediction Horizon

Xicai Liu, *Student Member, IEEE*, Jin Wang, *Member, IEEE*, Xiaonan Gao, *Member, IEEE*, Wei Tian, *Student Member, IEEE*, Libing Zhou, *Member, IEEE*, Jose Rodriguez, *Life Fellow, IEEE*, and Ralph Kennel, *Senior Member, IEEE*

***Abstract*—This article proposes a continuous control set predictive speed control (CCS-PSC) strategy for surface-mounted permanent magnet synchronous motor (SPMSM) drives, where the prediction horizon is short and the computational complexity is low. The optimization problem of the proposed CCS-PSC is formulated and analyzed. The current and voltage constraints are transformed into incremental voltage constraints, which can be updated in real-time. A reduced-order incremental model of SPMSM is adopted for the prediction, where integrators are naturally embedded. Hildreth's quadratic programming algorithm is used to solve the optimization problem, where the active constraints are identified and the reference voltage is calculated. The performance of the proposed strategy is validated through comparative experiments with finite control set predictive speed control (FCS-PSC), cascaded CCS-PSC and field-oriented control. The results demonstrate the superb dynamic performance of the proposed CCS-PSC strategy, while the phase current total harmonic distortion is relatively low.**

***Index Terms*—.**

ABBREVIATIONS

CB-PWM	Carrier-Based Pulse Width Modulation
CCS	Continuous Control Set
CCS-PSC	Continuous Control Set Predictive Speed Control
DB	Dead-Beat
FCS	Finite Control Set
FCS-MPC	Finite Control Set Model Predictive Control
FCS-PCC	Finite Control Set Predictive Current Control
FCS-PSC	Finite Control Set Predictive Speed Control
FCS-PTC	Finite Control Set Predictive Torque Control
FOC	Field-Oriented Control
MIMO	Multiple-Input Multiple-Output
MPC	Model Predictive Control
MTPA	Maximum Torque Per Ampere
PI	Proportional-Integral
PSC	Predictive Speed Control
PWM	Pulse Width Modulation
QP	Quadratic Program
SPMSM	Surface-Mounted Permanent Magnet Synchronous Machine
SSE	Steady-State Error
THD	Total Harmonic Distortion

Manuscript received May 16, 2021; revised August 25, 2021; accepted September 28, 2021. Date of publication October 11, 2021; date of current version May 23, 2022. This work was supported in part by the J. Rodriguez support of ANID through projects under Grant FB0008, Grant ACT192013, and Grant 1210208. Recommended for publication by Associate Editor U. Deshpande. *(Corresponding author: Jin Wang.)*

Xicai Liu, Jin Wang, and Libing Zhou are with the State Key Laboratory of Advanced Electromagnetic Engineering and Technology, School of Electrical and Electronic Engineering, Huazhong University of Science and Technology, Wuhan 430074, China (e-mail: xicai.liu@tum.de; hustwj@126.com; zlb@mail.hust.edu.cn).

Xiaonan Gao, Wei Tian, and Ralph Kennel are with the Institute for Electrical Drive Systems and Power Electronics, Technical University of Munich, 80333 Munich, Germany (e-mail: xiaonan.gao@tum.de; wei.tian@tum.de; ralph.kennel@tum.de).

Jose Rodriguez is with the Faculty of Engineering, Universidad Andres Bello, Santiago 8370146, Chile (e-mail: jose.rodriguez@unab.cl).

Color versions of one or more figures in this article are available at https://doi.org/10.1109/TPEL.2021.3118270.

Digital Object Identifier 10.1109/TPEL.2021.3118270

I. INTRODUCTION

IN THE past decades, model predictive control (MPC) has been intensively investigated in electrical drive systems, which can be categorized into finite control set-MPC (FCS-MPC) and continuous control set-MPC (CCS-MPC).

With intuitive principle, FCS-MPC utilizes the discrete nature of switching devices to achieve multiple control objectives [1]–[4]. The most common FCS-MPC strategies applied to electrical drives are finite control set predictive current control (FCS-PCC) [5]–[7] and finite control set predictive torque control (FCS-PTC) [8]–[12]. In FCS-PCC, the current tracking errors are evaluated, while in FCS-PTC, the torque and flux are controlled simultaneously. Generally, FCS-PCC and FCS-PTC are cascaded with an outer speed control loop, where the speed is controlled by proportional–integral (PI) controller. The bandwidth of the PI speed controller is relatively low, which impairs the speed response dynamics. Moreover, the disturbance rejection performance is poor. Although the disturbance rejection ability can be improved by implementing disturbance observer [13], [14], the tuning of the proportional gain remains an issue.

Recently, finite control set predictive speed control (FCS-PSC) has been proposed to replace the PI speed controller, where the switching states are directly selected [15]–[22]. In [15], attraction regions of the currents are defined to achieve maximum torque per ampere operation. The copper losses can be reduced, however, multiple weighting factors need to be tuned and speed overshoots are noticeable. In [16], the cost

function is designed, where the high frequency components of the current are penalized. The sampling interval should be small, which means this strategy could be prone to noises. In [17], a sliding manifold defines the evolution of the torque, where high frequency torque ripples can be suppressed. However, different norms are used in the cost function, which impairs the further improvement of its performance. In [18], steady-state range and transient-state range are defined, where the configuration of the cost function is related to the operation point. A large number of weighting factors should be designed and optimal transition point between steady-state and transient-state cannot be guaranteed. In [19], a PI speed controller is used to generate the q-axis reference current to achieve short prediction horizon. The q-axis current tracking error is evaluated in addition to the speed tracking error. With the PI speed controller, high frequency torque ripples are suppressed. Nonetheless, the evaluation of the speed and q-axis current in different terms leads to speed overshoots. Only one switching state is applied each sampling period in [15]–[19], the current ripples are relatively high in case of low sampling frequency. To reduce the current ripples, duty-ratio and multiple voltage vectors are used without increasing the sampling frequency [20], [21]. In [20], the duty-ratio is selected through different stages of enumerations. Although the current ripples are small, speed overshoots are observed. In [21], reference voltages are calculated through dead-beat (DB) concept, with which multiple voltage vectors are selected and then applied. The selection of voltage vectors should be modified in case of overcurrents. The modification process is accomplished through heuristic analysis, where the merits of MPC in handling constraints systematically are not fully exploited.

An alternative to FCS-PSC is continuous control set predictive speed control (CCS-PSC), where its outputs are continuous within the feasible region. An outstanding merit of CCS-PSC is the readiness to adopt pulsewidth modulation (PWM), through which the current quality could be improved. Sufficiently long prediction horizon is commonly used to capture the speed dynamics, since the mechanical time constant is large. Nonetheless, long prediction horizon does not naturally suppress speed oscillations/overshoots. Elaborate control parameters (e.g., weighting factors, sampling time, prediction horizon, control horizon) are required to suppress speed oscillations/overshoots. These speed oscillations/overshoots result in oscillations in the torque-related current. On the other hand, long prediction horizon also contributes to the increase of the computational complexity. The prediction horizon is selected considering the computational capability of the processor and control performance, which could be a compromised solution.

CCS-PSC can be realized with or without cascaded control structure. Cascaded CCS-PSC strategies with inner current control loop are proposed in [23]–[25]. The incentive of the cascaded structure is to predict and control the speed and currents separately. In this manner, the issue arising from the large time constant differences between the electrical- and the mechanical system is avoided. Nonetheless, the ability of MPC to realize multiple-input multiple-output (MIMO) control is not fully utilized. Moreover, the outer loop speed MPC should be tuned carefully to obtain a relatively smooth output, which is not trivial. The cascaded control structure can be eliminated, where the speed and currents are controlled simultaneously with a single cost function [26]. However, without adequate weighting factors, large speed overshoots can be observed albeit with long prediction horizon.

The computational complexity induced by long prediction horizon in CCS-PSC could be tackled by powerful processors with additional cost. The real issue is, what is a "sufficiently long" prediction horizon? The selection of the prediction horizon as well as the tuning of the combined weighting factors could be time consuming and challenging.

Based on the above considerations, we raised the following question: Is it possible to adopt a new CCS-PSC control scheme to bypass the necessity of long prediction horizon, without causing speed oscillations/overshoots? If possible, the design flexibility could be tremendously improved.

In this article, a CCS-PSC strategy with short prediction horizon is proposed to obtain low current ripples, while maintaining high dynamic response without speed overshoots or oscillations. The main contributions of this article can be summarized as following three points. First, the proposed strategy is realized without long prediction horizon, which means the design flexibility is improved and the computational burden is relatively low. Second, current and voltage constraints are transformed into respective incremental voltage constraints, which facilitates the handling of constraints. Third, reduced-order incremental model of SPMSM is used, where integral actions are inherently embedded. In this way, the steady-state error (SSE) in speed can be eliminated.

This article is organized as follows. First, the model of SPMSM is given and the principle of PSC with reduced-order SPMSM model is described. Second, the proposed CCS-PSC strategy is illustrated in detail. Third, the effectiveness of proposed CCS-PSC strategy is verified through comparative experimental implementations. Major implementation aspects are also discussed. Finally, conclusion is made based on the experimental results.

II. System Description and Principle of Predictive Speed Control With Reduced-Order SPMSM Model

In this section, the full-order SPMSM model is first given. Based on this full-order SPMSM model, the reduced-order SPMSM model is deduced. Subsequently, the principle of PSC with reduced-order SPMSM model is briefly introduced.

A. Full-Order SPMSM Model

The system dynamics of SPMSM in the synchronous rotating d–q frame can be expressed as follows:

$$\begin{cases} \frac{d}{dt}i_d &= -\frac{R_s}{L_s}i_d + \omega_e i_q + \frac{u_d}{L_s} \\ \frac{d}{dt}i_q &= -\frac{R_s}{L_s}i_q - \omega_e i_d + \frac{u_q}{L_s} - \frac{\omega_e \psi_f}{L_s} \\ J\frac{d}{dt}\omega_m &= T_e - T_L \end{cases} \tag{1}$$

where i_d and i_q represent the d-axis and q-axis stator current, respectively. u_d and u_q stand for stator input voltage on the d-axis and q-axis, respectively. R_s is the stator resistance, L_s is the stator inductance, ψ_f is the magnitude of the rotor flux linkage, J is the rotor inertia, ω_e is the electrical angular speed of the motor, ω_m is the mechanical angular speed of the motor, T_e is the electromagnetic torque, and $T_e = \frac{3}{2}p\psi_f i_q$, T_L is the load torque.

B. Principle of Predictive Speed Control With Reduced-Order SPMSM Model

As shown in [15]–[26], numerous PSC strategies have been proposed and the cost functions varied. The main challenge to PSC is posed by the large difference between the electrical- and mechanical time constant. The mechanical time constant is much larger than the electrical one, which means the dynamics of the currents are much faster than the mechanical speed. PSC without adequate cost function may result in severe torque and speed ripples.

In this section, PSC strategy based on reduced-order SPMSM model is introduced. To obtain reduced-order SPMSM model, equivalent speed tracking error is defined as [27], [28]

$$e_\omega = \eta_m \omega_{\text{err}} + \dot{\omega}_{\text{err}} \tag{2}$$

where $\omega_{\text{err}} = \omega_e^* - \omega_e$. ω_{err} is the tracking error of the electrical angular speed, η_m is a coefficient and $\eta_m > 0, \omega_e^*$ is the electrical angular reference speed.

Remark 1: Consider e_ω as the input and ω_{err} as the output, the transfer function of (2) can be expressed as

$$\frac{\omega_{err}(s)}{e_\omega(s)} = \frac{1}{\eta_m + s}. \tag{3}$$

It is obvious that ω_{err} can be controlled through the control of e_ω, where the dynamic response of the speed error can be adjusted by tuning η_m. In this manner, short prediction horizon is enabled since the speed and its derivative are controlled simultaneously. The goal of PSC with reduced-order SPMSM model is to keep the magnitude of e_ω as small as possible.

In PSC with reduced-order SPMSM model, the evolution of e_ω should be predicted, which means its derivative $\dot{e}_w$ should be known. The derivative of e_ω can be expressed as

$$\dot{e}_w = \eta_m \dot{w}_{\text{err}} + \ddot{w}_{\text{err}}. \tag{4}$$

Assuming $\dot{\omega}_e^* = \ddot{\omega}_e^* = 0$, $\dot{e}_w$ can be expressed as

$$\dot{e}_\omega = -\eta_m \dot{w}_e - \ddot{w}_e. \tag{5}$$

Substitute (1) into (5) and consider e_ω as state variable, the state dynamics of SPMSM with reduced-order are obtained

$$\begin{cases} \frac{d}{dt} e_w = -\frac{3p^2\psi_f}{2L_s J} u_q + g_w \\ \frac{d}{dt} i_d = \frac{1}{L_s} u_d + g_d \end{cases} \tag{6}$$

where

$$g_w = \frac{3p^2\psi_f}{2J}\left(\frac{R_s}{L_s} i_q + w_e i_d + \frac{\psi_f}{L_s} w_e - \eta_m i_q\right) + \frac{\eta_m p}{J} T_L$$

$$g_d = w_e i_q - \frac{R_s}{L_s} i_d.$$

Remark 2: The terms g_w and g_d in (6) are regarded as disturbances. These terms are normally calculated with the nominal parameters of the system and the accuracy of the calculations depends on the knowledge of the system.

In practical applications, (6) should be discretized to predict the evolution of e_ω and i_d. In this article, (6) is discretized with the forward Euler approximation

$$\begin{cases} e_\omega(k+1) = e_\omega(k) - \frac{3p^2\psi_f T_s}{2L_s J} u_q(k) + g_\omega(k) T_s \\ i_d(k+1) = i_d(k) + \frac{T_s}{L_s} u_d(k) + g_d(k) T_s. \end{cases} \tag{7}$$

For notational simplicity, (7) is described in vector form

$$\boldsymbol{x}(k+1) = \boldsymbol{x}(k) + \boldsymbol{H}\boldsymbol{U}_{dq}(k) + \boldsymbol{G}_\omega(k) \tag{8}$$

where

$$\boldsymbol{x}(k) = \begin{bmatrix} e_\omega(k) \\ i_d(k) \end{bmatrix}, \boldsymbol{H} = T_s \begin{bmatrix} -\frac{3p^2\psi_f}{2L_s J} & 0 \\ 0 & \frac{1}{L_s} \end{bmatrix},$$

$$\boldsymbol{U}_{dq}(k) = \begin{bmatrix} u_q(k) \\ u_d(k) \end{bmatrix}, \boldsymbol{G}_\omega(k) = \begin{bmatrix} g_\omega(k) T_s \\ g_d(k) T_s \end{bmatrix}.$$

The equivalent speed error dynamics e_ω and d-axis current i_d are controlled in a single cost function. Considering one-step computational delay, the cost function can be designed as

$$J = \boldsymbol{x}_e(k+2)^T \boldsymbol{W} \boldsymbol{x}_e(k+2) + k_u \Delta \boldsymbol{U}_{dq}(k+1)^T \Delta \boldsymbol{U}_{dq}(k+1) \tag{9}$$

subject to

$$(i_d^p(k+2))^2 + (i_q^p(k+2))^2 \le i_{\max}^2$$

$$(u_d(k+1))^2 + (u_q(k+1))^2 \le u_{\max}^2$$

where $\boldsymbol{x}_e(k+2) = \boldsymbol{x}^* - \boldsymbol{x}^p(k+2)$, $\boldsymbol{x}^p(k+2)$ is the predicted state vector at time instant $k+2$, $\boldsymbol{W} = \begin{bmatrix} k_\omega & 0 \\ 0 & k_{id} \end{bmatrix}$, $\Delta \boldsymbol{U}_{dq}(k+1) = \boldsymbol{U}_{dq}(k+1) - \boldsymbol{U}_{dq}(k)$, k_{id}, k_ω, and k_u are the weighting factors, respectively. $\boldsymbol{x}^* = [0, i_d^*]^T$, i_d^* is the d-axis reference current. $i_{\max}$ is the maximum allowable current magnitude, $u_{\max}$ is the maximum allowable voltage magnitude.

In cost function (9), the first term corresponds to the tracking errors and the second term is used to penalize the control effort. (9) can be used in FCS-PSC and CCS-PSC. For FCS-PSC, the admissible switching states are enumerated and the one which minimizes the cost function is selected and applied. For CCS-PSC, the optimization problem is a quadratic program (QP), which can be solved with QP solvers. The reference voltage is calculated with the selected QP solver and modulation techniques are used thereafter.

Remark 3: For FCS-PSC with cost function (9), the d-axis current i_d oscillates during acceleration transients. At the start of the acceleration, the equivalent speed tracking error is much larger than i_d current tracking error. The two-norm exacerbates such difference and the cost function tends to mainly penalize the equivalent speed tracking error, which means i_d is less controlled. To mitigate oscillations in i_d, 1-norm can be selected.

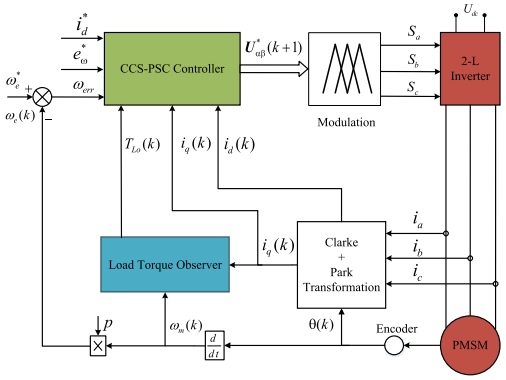

Fig. 1. Control diagram of the proposed CCS–PSC strategy.

III. Proposed CCS-PSC Strategy

The control diagram of the proposed CCS-PSC strategy is shown in Fig. 1. As depicted in the figure, the proposed CCS-PSC calculates the reference voltage $\boldsymbol{U}^*_{\alpha\beta}(k+1)$, which is then synthesized by selected modulation technique. The key elements of the proposed CCS-PSC strategy are: reduced-order incremental SPMSM model, reformulated current/voltage constraints, and the calculation of the constrained optimum.

A. Reduced-Order Incremental SPMSM Model

In (8), the calculation of g_w and g_d is parameter dependent. In case of parameter mismatches, g_w and g_d cannot be calculated accurately. To improve the robustness against variations of parameters, incremental form of (8) can be used

$$\Delta\boldsymbol{x}(k+1) = \Delta\boldsymbol{x}(k) + \boldsymbol{H}\Delta\boldsymbol{U}_{dq}(k) + \Delta\boldsymbol{G}_{\omega}(k) \tag{10}$$

where

$$\begin{aligned}\Delta\boldsymbol{x}(k+1) &= \boldsymbol{x}(k+1) - \boldsymbol{x}(k)\\ \Delta\boldsymbol{U}_{dq}(k) &= \boldsymbol{U}_{dq}(k) - \boldsymbol{U}_{dq}(k-1)\\ \Delta\boldsymbol{G}_{\omega}(k) &= \boldsymbol{G}_{\omega}(k) - \boldsymbol{G}_{\omega}(k-1).\end{aligned} \tag{11}$$

The system states $\boldsymbol{x}^p(k+2)$ at time instant $k+2$ can be predicted based on $\boldsymbol{x}^p(k+1)$ and $\Delta\boldsymbol{x}^p(k+2)$

$$\begin{bmatrix}\Delta\boldsymbol{x}^p(k+2)\\ \boldsymbol{x}^p(k+2)\end{bmatrix} = \begin{bmatrix}\boldsymbol{I}_2 & \boldsymbol{0}_2\\ \boldsymbol{I}_2 & \boldsymbol{I}_2\end{bmatrix}\begin{bmatrix}\Delta\boldsymbol{x}^p(k+1)\\ \boldsymbol{x}^p(k+1)\end{bmatrix} + \begin{bmatrix}\boldsymbol{I}_2\\ \boldsymbol{I}_2\end{bmatrix}\boldsymbol{H}\Delta\boldsymbol{U}_{\boldsymbol{dq}}(k+1) + \begin{bmatrix}\boldsymbol{I}_2\\ \boldsymbol{I}_2\end{bmatrix}\Delta\boldsymbol{G}_{\boldsymbol{\omega}}(k+1) \tag{12}$$

Note that the vectors/variables with superscript p are predicted values.

Remark 4: Since incremental model is used in the prediction of $\boldsymbol{x}^p(k+2)$, integral actions are inherently embedded, which can be explained by the eigenvalues of (12). The eigenvalues can be calculated by setting its characteristic polynomial to zero

$$\det\left[(\lambda-1)\boldsymbol{I_2}\cdot(\lambda-1)\boldsymbol{I_2}\right] = 0. \tag{13}$$

It can be seen from (13) that all of the eigenvalues of (12) are 1. Two eigenvalues originate from (8) and the other two are from the incremental model, which means two integrators are incorporated through the incremental prediction. In this manner, the robustness of the system against parameter mismatches is improved.

For notational simplicity, $\boldsymbol{x}^p(k+2)$ can be also expressed as

$$\boldsymbol{x}^p(k+2) = \boldsymbol{\sigma}(k+1) + \boldsymbol{H}\Delta\boldsymbol{U}_{dq}(k+1) \tag{14}$$

where

$$\boldsymbol{\sigma}(k+1) = \boldsymbol{x}^p(k+1) + \Delta\boldsymbol{G}_{\omega}(k+1) + \boldsymbol{H}\Delta\boldsymbol{U}_{dq}(k).$$

B. Unconstrained Optimization

Without considering system constraints, the unconstrained optimization problem is to calculate $\Delta\boldsymbol{U}_{dq,unc}(k+1)$, which minimizes cost function (9)

$$\Delta\boldsymbol{U}_{dq,unc}(k+1) = \arg\min_{\Delta\boldsymbol{U}_{dq}} J. \tag{15}$$

Substitute (14) into (9), the cost function (9) can be reformulated as

$$\begin{aligned}J = {}&\Delta\boldsymbol{U}_{dq}^T(k+1)(\boldsymbol{H}^T\boldsymbol{W}\boldsymbol{H} + k_u\boldsymbol{I}_2)\Delta\boldsymbol{U}_{dq}(k+1)\\ &- 2\Delta\boldsymbol{U}_{dq}^T(k+1)\boldsymbol{H}^T\boldsymbol{W}(\boldsymbol{x}^* - \boldsymbol{\sigma}(k+1))\\ &+ (\boldsymbol{x}^* - \boldsymbol{\sigma}(k+1))^T\boldsymbol{W}(\boldsymbol{x}^* - \boldsymbol{\sigma}(k+1))\end{aligned} \tag{16}$$

where $\boldsymbol{I}_2$ is unit diagonal matrix.

Since $\boldsymbol{H}^T\boldsymbol{W}\boldsymbol{H} + k_u\boldsymbol{I}_2$ is positive definite, J can be minimized if $\Delta\boldsymbol{U}_{dq}$ satisfies the following condition:

$$\begin{aligned}\frac{\partial J}{\partial\Delta\boldsymbol{U}_{dq}} = {}&2(\boldsymbol{H}^T\boldsymbol{W}\boldsymbol{H} + k_u\boldsymbol{I}_2)\Delta\boldsymbol{U}_{dq}(k+1)\\ &- 2\boldsymbol{H}^T\boldsymbol{W}(\boldsymbol{x}^* - \boldsymbol{\sigma}(k+1)) = 0.\end{aligned} \tag{17}$$

By solving (17), the unconstrained optimum can be expressed as

$$\begin{aligned}&\Delta\boldsymbol{U}_{dq,unc}(k+1)\\ &= (\boldsymbol{H}^T\boldsymbol{W}\boldsymbol{H} + k_u\boldsymbol{I}_2)^{-1}\boldsymbol{H}^T\boldsymbol{W}(\boldsymbol{x}^* - \boldsymbol{\sigma}(k+1)).\end{aligned} \tag{18}$$

C. Current Constraints

The magnitudes of the currents should be constrained to prevent overcurrent. Otherwise, it could lead to motor and inverter damages. Conventionally, the current constraint is formulated as

$$i_d^2(k+2) + i_q^2(k+2) \le i_{\max}^2. \tag{19}$$

In practice, overcurrent usually occurs during the acceleration or deceleration, where the q-axis current violates (19). Therefore, current constraints can be imposed separately on individual current:

$$\begin{cases} i_d^2(k+2) \le i_{d,\max}^2\\ i_q^2(k+2) \le i_{q,\max}^2\\ i_{d,\max}^2 + i_{q,\max}^2 = i_{\max}^2\end{cases}. \tag{20}$$

Since incremental model is used in the prediction, (20) is transformed into the constraints of incremental currents

$$\begin{cases} \Delta i_d(k+2) & \le i_{d,\max} - i_d(k+1)\\ -\Delta i_d(k+2) & \le i_{d,\max} + i_d(k+1)\\ \Delta i_q(k+2) & \le i_{q,\max} - i_q(k+1)\\ -\Delta i_q(k+2) & \le i_{q,\max} + i_q(k+1)\\ i_{d,\max}^2 + i_{q,\max}^2 & = i_{\max}^2\end{cases} \tag{21}$$

where

$$\begin{cases} \Delta i_d(k+2) = \frac{T_s}{L_s}\Delta u_d(k+1) + a \\ \Delta i_q(k+2) = \frac{T_s}{L_s}\Delta u_q(k+1) + b \end{cases} \tag{22}$$

and

$$a = \left(1 - \frac{R_s T_s}{L_s}\right)\Delta i_d(k+1) + \omega_e(k+1)\Delta i_q(k+1)T_s$$

$$b = \left(1 - \frac{R_s T_s}{L_s}\right)\Delta i_q(k+1) - \omega_e(k+1)\Delta i_d(k+1)T_s.$$

Substituting (22) into (21) yields

$$\begin{cases} \Delta u_d(k+1) & \le \frac{L_s}{T_s}(i_{d,\max} - i_d(k+1) - a) \\ -\Delta u_d(k+1) & \le \frac{L_s}{T_s}(i_{d,\max} + i_d(k+1) + a) \\ \Delta u_q(k+1) & \le \frac{L_s}{T_s}(i_{q,\max} - i_q(k+1) - b) \\ -\Delta u_q(k+1) & \le \frac{L_s}{T_s}(i_{q,\max} + i_q(k+1) + b) \\ i_{d,\max}^2 + i_{q,\max}^2 = i_{\max}^2. \end{cases} \tag{23}$$

In this way, the current constraints (21) are transformed into the incremental voltage constraints (23), which means $\Delta u_d(k+1)$ and $\Delta u_q(k+1)$ can be constrained to prevent overcurrents.

D. Voltage Constraints

The magnitudes of the voltages should be constrained to meet the inverter output capability, which is dependent on the dc-link voltage and the selected modulation method. Without overmodulation, the voltage constraint can be expressed as

$$u_d^2(k+1) + u_q^2(k+1) \le \left(\frac{1}{\sqrt{3}}U_{\text{dc}}\right)^2 \tag{24}$$

where U_{dc} is the dc-link voltage.

For time instant $k+1$, the voltage constraint is

$$(u_d(k)+\Delta u_d(k+1))^2 + (u_q(k)+\Delta u_q(k+1))^2 \le \left(\frac{U_{\text{dc}}}{\sqrt{3}}\right)^2. \tag{25}$$

In this article, (25) is used to identify whether the unconstrained optimum (18) violates voltage constraints. In case of violation, the voltage constraints can be imposed on $\Delta u_d(k+1)$ and $\Delta u_q(k+1)$ separately

$$\begin{cases} |u_q(k) + \Delta u_q(k+1)| & \le \frac{\frac{U_{\text{dc}}}{\sqrt{3}}|u_q(k)+\Delta u_{q,unc}(k+1)|}{\|\boldsymbol{U}_{dq}(k)+\Delta\boldsymbol{U}_{dq,unc}(k+1)\|} \\ |u_d(k) + \Delta u_d(k+1)| & \le \frac{\frac{U_{\text{dc}}}{\sqrt{3}}|u_d(k)+\Delta u_{d,unc}(k+1)|}{\|\boldsymbol{U}_{dq}(k)+\Delta\boldsymbol{U}_{dq,unc}(k+1)\|} \end{cases}. \tag{26}$$

The rewrite of (26) yields

$$\begin{cases} \Delta u_q(k+1) & \le \frac{\frac{U_{\text{dc}}}{\sqrt{3}}|u_q(k)+\Delta u_{q,unc}(k+1)|}{\|\boldsymbol{U}_{dq}(k)+\Delta\boldsymbol{U}_{dq,unc}(k+1)\|} - u_q(k) \\ -\Delta u_q(k+1) & \le \frac{\frac{U_{\text{dc}}}{\sqrt{3}}|u_q(k)+\Delta u_{q,unc}(k+1)|}{\|\boldsymbol{U}_{dq}(k)+\Delta\boldsymbol{U}_{dq,unc}(k+1)\|} + u_q(k) \\ \Delta u_d(k+1) & \le \frac{\frac{U_{\text{dc}}}{\sqrt{3}}|u_d(k)+\Delta u_{d,unc}(k+1)|}{\|\boldsymbol{U}_{dq}(k)+\Delta\boldsymbol{U}_{dq,unc}(k+1)\|} - u_d(k) \\ -\Delta u_d(k+1) & \le \frac{\frac{U_{\text{dc}}}{\sqrt{3}}|u_d(k)+\Delta u_{d,unc}(k+1)|}{\|\boldsymbol{U}_{dq}(k)+\Delta\boldsymbol{U}_{dq,unc}(k+1)\|} + u_d(k) \end{cases}. \tag{27}$$

Remark 5: If the unconstrained optimum (18) satisfies (25), it will definitely satisfy (26). Therefore, (27) is used as voltage constraints.

E. Constrained Optimizaion

After transforming current constraints (20) and voltage constraints (25) into incremental voltage constraints (27) and (23), the constrained optimization can be reformulated as

$$\Delta\boldsymbol{U}_{dq,\text{cons}}(k+1) = \arg\min_{\Delta\boldsymbol{U}_{dq}} J \tag{28}$$

subject to

$$\boldsymbol{\Phi}\Delta\boldsymbol{U}_{dq}(k+1) \le \boldsymbol{\gamma}$$

where

$$\boldsymbol{\Phi} = \begin{bmatrix} 1 & 0 \\ -1 & 0 \\ 0 & 1 \\ 0 & -1 \\ 1 & 0 \\ -1 & 0 \\ 0 & 1 \\ 0 & -1 \end{bmatrix}$$

$$\boldsymbol{\gamma} = \begin{bmatrix} \frac{L_s}{T_s}(i_{q,\max} - i_q(k+1) - a) \\ \frac{L_s}{T_s}(i_{q,\max} + i_q(k+1) + a) \\ \frac{L_s}{T_s}(i_{d,\max} - i_d(k+1) - b) \\ \frac{L_s}{T_s}(i_{d,\max} + i_d(k+1) + b) \\ \frac{\frac{1}{\sqrt{3}}U_{\text{dc}}|u_q(k)+\Delta u_{q,unc}(k+1)|}{\|\boldsymbol{U}_{dq}(k)+\Delta\boldsymbol{U}_{dq,unc}(k+1)\|} - u_q(k) \\ \frac{\frac{1}{\sqrt{3}}U_{\text{dc}}|u_q(k)+\Delta u_{q,unc}(k+1)|}{\|\boldsymbol{U}_{dq}(k)+\Delta\boldsymbol{U}_{dq,unc}(k+1)\|} + u_q(k) \\ \frac{\frac{1}{\sqrt{3}}U_{\text{dc}}|u_d(k)+\Delta u_{d,unc}(k+1)|}{\|\boldsymbol{U}_{dq}(k)+\Delta\boldsymbol{U}_{dq,unc}(k+1)\|} - u_d(k) \\ \frac{\frac{1}{\sqrt{3}}U_{\text{dc}}|u_d(k)+\Delta u_{d,unc}(k+1)|}{\|\boldsymbol{U}_{dq}(k)+\Delta\boldsymbol{U}_{dq,unc}(k+1)\|} + u_d(k) \end{bmatrix}.$$

Constrained optimization problem (28) is called the primal problem, which is equivalent to the dual problem

$$\max_{\boldsymbol{\lambda}\ge 0}\min_{\Delta\boldsymbol{U}_{dq}}\left[\frac{1}{2}J + \boldsymbol{\lambda}^T(\boldsymbol{\Phi}\Delta\boldsymbol{U}_{dq} - \boldsymbol{\gamma})\right] \tag{29}$$

where $\boldsymbol{\lambda}$ is the Lagrange multiplier.

With the minimizaton over $\Delta\boldsymbol{U}_{dq}$, the dual problem (29) is equivalent to

$$\max_{\boldsymbol{\lambda}\ge 0}(-\frac{1}{2}\boldsymbol{\lambda}^T E\boldsymbol{\lambda} - \boldsymbol{\lambda}^T\boldsymbol{F} - \frac{1}{2}\boldsymbol{\gamma}^T(\boldsymbol{H}^T\boldsymbol{W}\boldsymbol{H} + k_u\boldsymbol{I}_2)^{-1}\boldsymbol{\gamma}) \tag{30}$$

where

$$\boldsymbol{E} = \boldsymbol{\Phi}(\boldsymbol{H}^T\boldsymbol{W}\boldsymbol{H} + k_u\boldsymbol{I}_2)\boldsymbol{\Phi}^T$$

$$\boldsymbol{F} = \boldsymbol{\gamma} - \boldsymbol{\Phi}(\boldsymbol{H}^T\boldsymbol{W}\boldsymbol{H} + k_u\boldsymbol{I}_2)^{-1}\boldsymbol{H}^T\boldsymbol{W}(\boldsymbol{x}^* - \boldsymbol{\sigma}(k+1)).$$

$\Delta\boldsymbol{U}_{dq,\text{cons}}(k+1)$ can be obtained through solving the dual problem (29).

In this paper, Hildreth's quadratic programming algorithm is used to solve the dual problem (29). Iterative calculations are used to obtain $\boldsymbol{\lambda}$. Once $\boldsymbol{\lambda}$ is obtained, $\Delta\boldsymbol{U}_{dq,\text{corr}}(k+1)$ as well

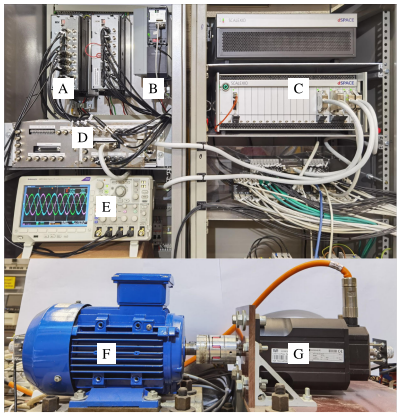

Fig. 2. Setup of the electrical drives testbench. A: SEW Inverter for PMSM, B: Danfoss Inverter for load induction machine (IM), C: dSPACE SCALEXIO real-time control system, D: Interface, E: Oscilloscope, F: IM, G: PMSM.

as $\Delta \boldsymbol{U}_{dq,\text{cons}}(k+1)$ can be calculated

$$\Delta \boldsymbol{U}_{dq,\text{cons}}(k+1) = \Delta \boldsymbol{U}_{dq,unc}(k+1) + \Delta \boldsymbol{U}_{dq,\text{corr}}(k+1) \tag{31}$$

where $\Delta \boldsymbol{U}_{dq,\text{corr}}(k+1)$ is the correction term

$$\Delta \boldsymbol{U}_{dq,\text{corr}}(k+1) = (\boldsymbol{H}^T \boldsymbol{W} \boldsymbol{H} + k_u \boldsymbol{I}_2)^{-1} \boldsymbol{\Phi}^T \boldsymbol{\lambda} \tag{32}$$

For more details of Hildreth's quadratic programming algorithm, the reader is referred to [26]. After obtaining $\Delta \boldsymbol{U}_{dq,\text{cons}}(k+1)$, the reference voltage in the synchronous rotating d–q frame can be expressed as

$$\boldsymbol{U}^*_{dq}(k+1) = \Delta \boldsymbol{U}_{dq,\text{cons}}(k+1) + \boldsymbol{U}_{dq}(k). \tag{33}$$

With the inverse Park transformation, the reference voltage in the stationary α–β frame can be written as

$$\boldsymbol{U}^*_{\alpha\beta}(k+1) = \boldsymbol{K}^{-1}_{\alpha\beta} \boldsymbol{U}^*_{dq}(k+1) \tag{34}$$

where

$$\boldsymbol{K}^{-1}_{\alpha\beta} = \begin{bmatrix} -\sin(\theta) & \cos(\theta) \\ \cos(\theta) & \sin(\theta) \end{bmatrix}.$$

Carrier-based pulsewidth modulation (CB-PWM) is then used to synthesize $\boldsymbol{U}^*_{\alpha\beta}(k+1)$ and the three phase duty-cycles S_a, S_b, S_c are obtained.

IV. Experimental Results

In this section, dynamic as well as steady-state performances of the proposed CCS-PSC are experimentally studied. Comparative experiments with FCS-PSC, cascaded CCS-PSC [23], and FOC are also implemented. The experimental setup is shown in Fig. 2. A SPMSM driven by a SEW inverter is used as the test motor, which is controlled by a dSPACE SCALEXIO real-time controller. Nominal parameters of the SPMSM are listed in Table I. An induction motor is used as the load motor, which is fed by a Danfoss inverter and mechanically coupled with the SPMSM.

The sampling frequency is set to 20 kHz and the dc-link voltage is 560 V for all the tests. For the proposed CCS-PSC, cascaded CCS-PSC, as well as FOC, CB-PWM is used. The carrier frequency and the switching frequency are both 10 kHz.

TABLE I
SPMSM Nominal Parameters

Parameter	Value
Nominal Stator Resistance R_s [Ohm]	1.65
Nominal Stator Inductance L_s [mH]	9.8
Nominal Rotor Flux Linkage ψ_f [Wb]	0.26
Rated Current I_n [A]	6.3
Rated Speed N_n [r/min]	3000
Rated Voltage V_n [V]	380
Motor Pole Pairs N_p [1]	3
Drive System Inertia J [Kgm^2]	3.42e-3

TABLE II
Control Parameters Used in FCS-PSC and the Proposed CCS-PSC

Control scheme	k_{id}	k_ω	k_u	η_m
FCS-PSC	1	3.3e-3	0	80
Proposed CCS-PSC	1	1.6e-7	1e-4	80

TABLE III
Control Parameters Used in Cascaded CCS-PSC

	Q	R	Prediction horizon
Speed MPC	2.5	5	12
Current MPC	1	1e-4	2

The maximum allowable currents in the proposed CCS-PSC, cascaded CCS-PSC, and FCS-PSC are set to ± 10 A, while the output limits of the PI speed controller in FOC are ± 10.2 A. In FCS-PSC, the proposed CCS-PSC and cascaded CCS-PSC, the load torque is estimated with the Kalman-filter. For more details of load torque estimation using Kalman-filter, the reader is referred to [17]. The control parameters used in FCS-PSC and the proposed CCS-PSC are listed in Table II. It should be noted that 1-norm cost function is used in FCS-PSC to suppress i_d oscillations during acceleration transients, while 2-norm cost function is used in the proposed CCS-PSC. The weighting factors and prediction horizon of different loops in cascaded CCS-PSC are summarized in Table III. The parameter Q refers to the weight on the tracking performance, while R is used to penalize the variation of the control action.

A. Comparison of Dynamic Performances

1) Acceleration Performances: Fig. 3 shows the acceleration performances of four control schemes: FCS-PSC, the proposed CCS-PSC, cascaded CCS-PSC, and FOC. The motor accelerates from standstill to 2000 r/min while the load torque is not actively applied. For FCS-PSC and the proposed CCS-PSC, fast speed transient performance with no overshoots is achieved (settling time: 0.086 s and 0.083 s, respectively.) The q-axis current i_q stays at the maximum allowable current of 10 A at the initial stage of the acceleration and decreases smoothly as the system approaches steady-state, respectively. For cascaded CCS-PSC, the speed accelerates to the reference speed aggressively (settling time: 0.064 s). The current i_q stays at 10 A during the acceleration and decreases drastically once the reference speed is reached. Oscillations in i_q are observed as the acceleration ends. Different to FCS-PSC and the proposed CCS-PSC, large speed overshoots (50 r/min, 2.5% of reference speed) and longer settling time (0.091 s) are observed with FOC. Even at the

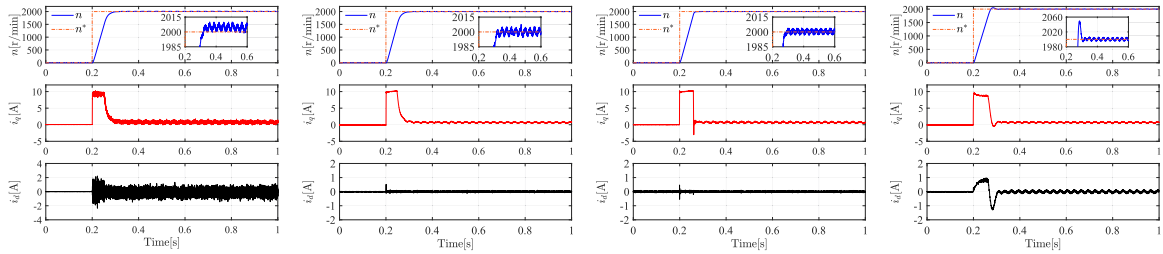

Fig. 3. [Experimental results:] Comparative acceleration performances, for each figure-set, from up to down are: motor speed, q-axis current, d-axis current, respectively. (a) FCS-PSC. (b) Proposed CCS-PSC. (c) Cascaded CCS-PSC. (d) FOC.

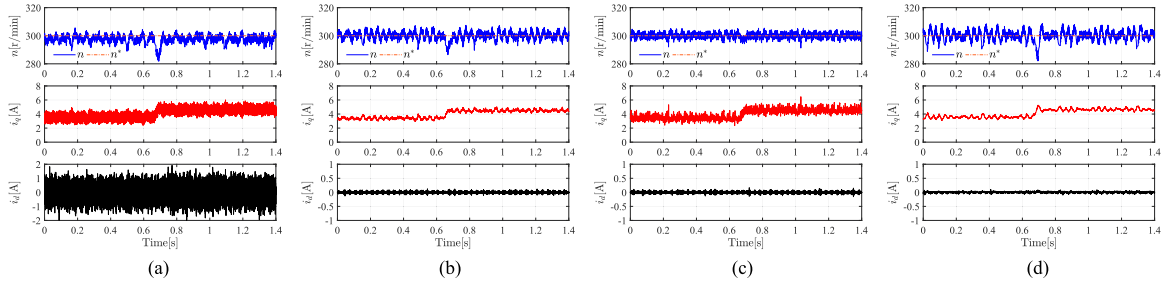

Fig. 4. [Experimental results:] Comparative dynamic responses under load torque disturbance at low speed operation, for each figure-set, from up to down are: motor speed, q-axis current, d-axis current, respectively. (a) FCS-PSC. (b) Proposed CCS-PSC. (c) Cascaded CCS-PSC. (d) FOC.

TABLE IV
COMPARATIVE ACCELERATION PERFORMANCES

	FCS-PSC	Proposed CCS-PSC	Cascaded CCS-PSC	FOC
Speed settling time [s]	0.086	0.083	0.064	0.091
Speed overshoot [r/min]	0	0	0	50
SSE of speed [r/min]	3.7	0	0	0

TABLE V
COMPARATIVE PERFORMANCES UNDER LOAD TORQUE DISTURBANCE AT LOW SPEED OPERATION

	FCS-PSC	Proposed CCS-PSC	Cascaded CCS-PSC	FOC
Speed settling time [s]	0.06	0.06	0.06	0.08
Speed drop [r/min]	15.6	13.5	5.7	17.8
SSE of speed [r/min]	2.6	0	0	0
Speed ripple [r/min] (B/A)	15.7/13.3	12.6/14.5	9.6/9.9	17.7/16.7
i_q ripple [A] (B/A)	2.37/2.32	0.99/0.92	1.71/1.74	1.05/0.79
i_d ripple [A] (B/A)	3.51/3.63	0.18/0.17	0.21/0.23	0.11/0.12

beginning of the acceleration, i_q is not able to reach the upper limit of the PI speed controller. Large disturbances are also observed in i_d during the acceleration. To improve the acceleration performance of FOC, elaborate decoupling mechanisms should be designed.

Comparative acceleration performances of the four schemes are summarized in Table IV. It should be noted that SSE in speed is observed with FCS-PSC, while no SSEs in speed are observed with FOC, the proposed CCS-PSC and cascaded CCS-PSC. FCS-PSC is a method with high feedback gain and SSE in speed occurs in case of model mismatches, which is normally the case. In the proposed CCS-PSC, incremental model is used and integrator is naturally embedded, which eliminates the SSE in speed. In cascaded CCS-PSC, the lumped disturbance in the speed loop is estimated by the Kalman-filter and is compensated by the speed MPC. In FOC, the integral action of the speed controller eliminates the speed SSE.

2) Dynamic Responses Under Load Torque Disturbance at Low Speed Operation: Fig. 4 shows the load torque disturbance rejection abilities of the four control schemes at low speed operation: FCS-PSC, the proposed CCS-PSC, cascaded CCS-PSC, and FOC. The speed reference is 300 r/min. At the time instant 0.65 s, the reference load torque changes from 4 to 5 N·m. The rising time of the load torque is 50 ms. For FCS-PSC and the proposed CCS-PSC, the dynamic performances are almost the same and the speed recovers very quickly thanks to the load torque observer. The load torque is observed by the Kalman-filter and its feed-forward compensation is included in the prediction. SSE of 2.6 r/min in the speed can be observed with FCS-PSC, which is not the case with the proposed CCS-PSC. For cascaded

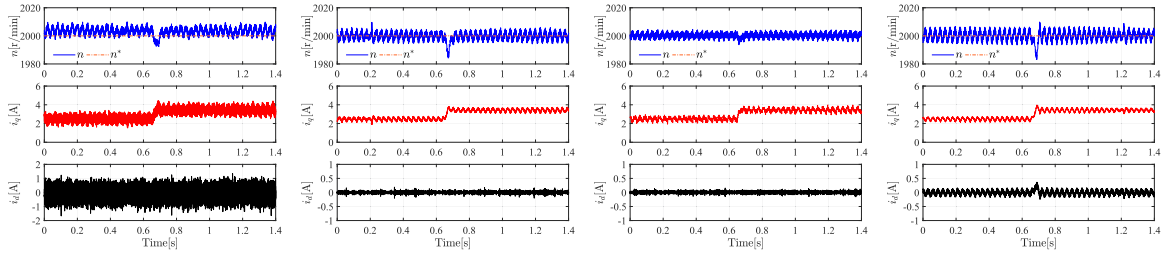

Fig. 5. [Experimental results:] Comparative dynamic responses under load torque disturbance at high speed operation, for each figure-set, from up to down are: motor speed, q-axis current, d-axis current, respectively. (a) FCS-PSC. (b) Proposed CCS-PSC. (c) Cascaded CCS-PSC. (d) FOC.

TABLE VI
COMPARATIVE PERFORMANCES UNDER LOAD TORQUE DISTURBANCE AT HIGH SPEED OPERATION

	FCS-PSC	Proposed CCS-PSC	Cascaded CCS-PSC	FOC
Speed settling time [s]	0.06	0.06	0.06	0.08
Speed drop [r/min]	11.6	15.7	6.3	16.2
SSE of speed [r/min]	−3.3	0	0	0
Speed ripple [r/min] (B/A)	11.4/12.9	10.5/10.3	7.7/7.6	11.5/12.1
i_q ripple [A] (B/A)	1.72/1.90	0.93/0.64	0.97/1.02	0.55/0.59
i_d ripple [A] (B/A)	2.90/2.91	0.29/0.28	0.24/0.28	0.34/0.35

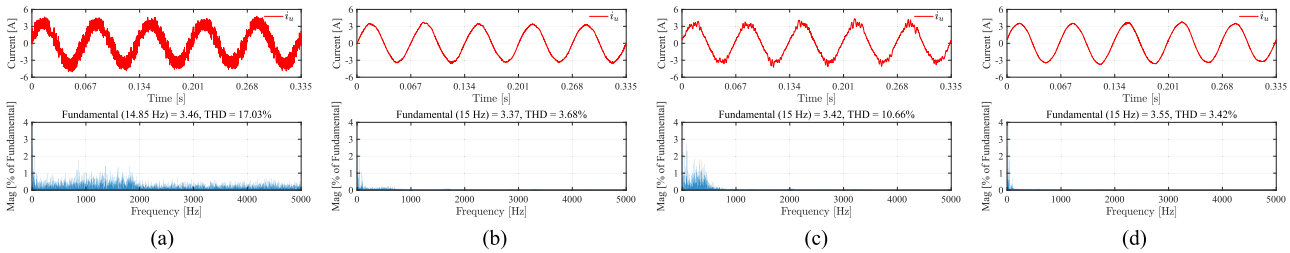

Fig. 6. [Experimental results:] Comparative steady-state performances at low speed operation, for each figure-set, from up to down are: phase current, THD of phase current, respectively. (a) FCS-PSC. (b) Proposed CCS-PSC. (c) Cascaded CCS-PSC. (d) FOC.

CCS-PSC, very small speed drop (5.7 r/min) is observed thanks to its high bandwidth speed MPC and the Kalman-filter. For FOC, the speed recovers slower and the settling time is 0.08 s. The lack of feed-forward load torque compensation leads to poor disturbance rejection ability. The speed recovers mainly due to the integral action of the speed PI controller. Comparative performances of the four schemes under load torque disturbance at low speed operation are listed in Table V. The speed and current ripples before and after (B/A) the load torque application are also included. Smallest speed ripples are obtained with cascaded CCS-PSC at the cost of distorted q-axis current. The speed ripples with FOC is larger than that with the proposed CCS-PSC, while comparable current ripples in i_q and i_d are obtained.

3) Dynamic Responses Under Load Torque Disturbance at High Speed Operation: Fig. 5 illustrates the load torque disturbance rejection performances of the four control schemes (i.e., FCS-PSC, the proposed CCS-PSC, cascaded CCS-PSC, and FOC) at high speed operation. The speed reference is set to 2000 r/min. At the time instant 0.65 s, the reference load torque changes from 3 to 4 N·m. The rising time of the load torque is 50 ms. Compared with Fig. 4, similar transient performances are observed. Once again, the proposed CCS-PSC exhibits very similar dynamic performance with FCS-PSC (settling time 0.06 s). The cascaded CCS-PSC exhibits the smallest speed drop (6.3 r/min). On the contrary, largest speed drop (16.2 r/min) and slowest dynamic performance of the speed (settling time 0.08 s) are observed with FOC. Comparative performances of the four schemes under load torque disturbance at high speed operation are listed in Table VI.

B. Comparison of Steady-State Performances

1) Steady-State Performances at Low Speed Operation: In Fig. 6, steady-state performances of the four schemes (i.e., FCS-PSC, the proposed CCS-PSC, cascaded CCS-PSC, and FOC) at low speed operation are shown. The speed reference is 300 r/min and the load torque is 4 N·m. With a switching frequency of 2.24 kHz, the current ripples and current THD (17.03%) with FCS-PSC are the largest among the four control schemes. At low speed operation, the back-EMF is relatively small and the phase voltage variations between consecutive sampling instants are large with FCS-PSC, which leads to large current ripples.

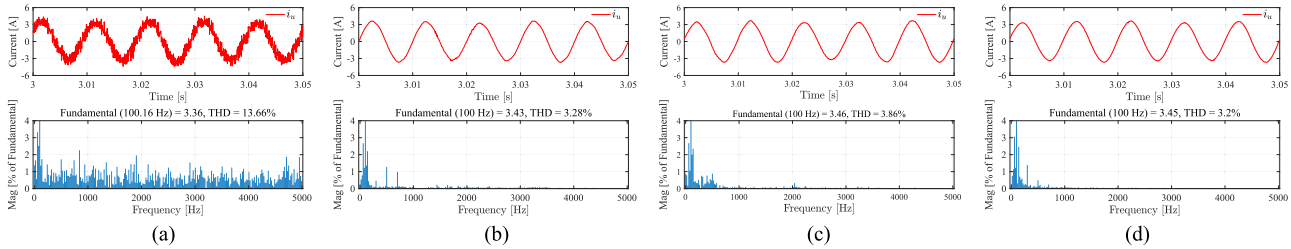

Fig. 7. [Experimental results:] Comparative steady-state performances at high speed operation, for each figure-set, from up to down are: phase current, THD of phase current, respectively. (a) FCS-PSC. (b) Proposed CCS-PSC. (c) Cascaded CCS-PSC. (d) FOC.

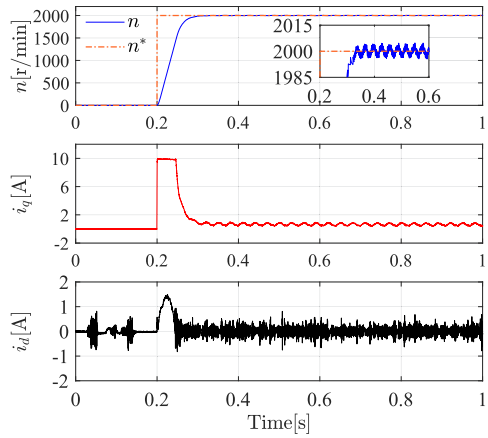

Fig. 8. [Experimental results:] Acceleration performance of the proposed CCS-PSC with $k_u = 0$, from up to down are: motor speed, q-axis current, d-axis current, respectively.

With the proposed CCS-PSC, current THD is reduced to 3.68%. For cascaded CCS-PSC, the phase current is distorted and its THD is 10.66%. The phase spectrum is corrupted with low frequency components up to 1 kHz, which originate from the q-axis reference current given by the outer speed loop. For FOC, the current THD (3.42%) is the smallest among all the control schemes.

2) Steady-State Performances at High Speed Operation: Fig. 7 illustrates the steady-state performances of the four control schemes (i.e., FCS-PSC, the proposed CCS-PSC, cascaded CCS-PSC, and FOC) at high speed operation. The speed reference is 2000 r/min and the load torque is 4 N · m. As can be seen from the figure, all of the steady-state performances with the four schemes are improved compared to those in Fig. 6. With FCS-PSC, large phase current ripples are still observed and the current THD is reduced from 17.03% to 13.66%. The reason is partly the increase of switching frequency (from 2.24 to 4.67 kHz). Another reason is the smaller phase voltage variations between consecutive sampling instants. The fundamental frequency of the phase current is 100.16 Hz due to SSE in the speed. With the proposed CCS-PSC, phase current ripples are suppressed and the current THD is reduced from 3.68% to 3.28%, with the same switching frequency of 10 kHz. Compared to FCS-PSC, the proposed CCS-PSC is preferred at high speed operations. The switching frequency with the proposed CCS-PSC is only 2.14 times of that with FCS-PSC, but the current THD reduces to 1/4.16 times of that with the FCS-PSC (In this case, reference speed is 2000 r/min). For cascaded CCS-PSC, the current THD is slightly higher than that with the proposed CCS-PSC. Harmonics between 400 and 600 Hz are clearly seen in the phase spectrum. The current THD with FOC are the smallest among the four schemes due to the low-bandwidth of the speed PI controller. The q-axis reference current contains few harmonics. On the contrary, for FCS-PSC and the proposed CCS-PSC, speed harmonics are reflected in the phase spectra since the speed and the q-axis current are controlled in the same term. For cascaded CCS-PSC, the high bandwidth outer loop speed MPC generates q-axis reference current filled with harmonics, which contributes to the rise of the current THD.

Remark 6: It should be clarified whether it is reasonable to compare FCS-PSC with CCS-PSC (specifically, the proposed CCS-PSC and cascaded CCS-PSC) and FOC under different switching frequencies. Indeed, one may prefer to compare them under the same switching frequency. However, it is impossible to increase/decrease the switching frequency with FCS-PSC, CCS-PSC, and FOC, while maintaining their intrinsic merits at the same time. Moreover, the control parameters (e.g., weighting factors, PI coefficients) have significant impact on the control performances. Generally speaking, FCS-PSC is a special application of FCS-MPC, which means FCS-PSC has common characteristics with FCS-MPC. For FCS-MPC, the switching frequency is dependent on the operating point, the sampling frequency and the weighting factors. Meanwhile, the performances of CCS-PSC and FOC are directly related to the CB-PWM. Hence, the comparison between FCS-MPC and CB-PWM could give us some insights, although not complete. It has been shown in [29] that at low switching frequency operations, FCS-MPC performs better than CB-PWM. Above certain switching frequency, the CB-PWM is superior to FCS-MPC. It implies that the current THD with FCS-PSC could be smaller than that with CCS-PSC and FOC, when the switching frequency is below certain threshold value. This threshold value varies for different controller settings. Even the change of the sampling time yields a different threshold value. Based on the above considerations, the purpose of the comparisons in Figs. 6 and 7 is to show the properties of the four control schemes rather than find a certain threshold value.

TABLE VII
COMPUTATION TIME OF THE PROPOSED CCS-PSC AND CASCADED CCS-PSC IN SCALEXIO REAL-TIME CONTROLLER

	Proposed CCS-PSC	Cascaded CCS-PSC
Computation time [μs]	2.6	16.6

V. IMPLEMENTATION ASPECTS

In this section, implementation aspects of the proposed CCS-PSC are investigated. The computational burden, noise immunity as well as the robustness against parameter mismatches in inertia are discussed in detail.

A. Computational Burden

As can be seen in (31), the unconstrained solution $\Delta \boldsymbol{U}_{dq,unc}(k+1)$ and correction term $\Delta \boldsymbol{U}_{dq,\text{corr}}(k+1)$ are used to obtain constrained solution $\Delta \boldsymbol{U}_{dq,\text{cons}}(k+1)$. Note that the calculation of $\Delta \boldsymbol{U}_{dq,\text{corr}}$ is based on the Lagrange multiplier $\boldsymbol{\lambda}$, which is obtained through iterative computations.

Obviously, matrix operations and iterative computations constitute to the main computational burden. The matrix operations are computationally cheap, since the highest order of the matrices is 2. For the iterations, the Lagrange multiplier is updated element to element

$$\boldsymbol{\lambda}_i^{m+1} = \max(0, \boldsymbol{\xi}_i^{m+1}) \tag{35}$$

and

$$\boldsymbol{\xi}_i^{m+1} = -\frac{1}{\boldsymbol{E}_{ii}} \left[\boldsymbol{F}_i + \sum_{j=1}^{i-1} \boldsymbol{E}_{ij} \boldsymbol{\lambda}_j^{m+1} + \sum_{j=i+1}^{n} \boldsymbol{E}_{ij} \boldsymbol{\lambda}_j^{m} \right] \tag{36}$$

where the subscripts correspond to indices of respective matrix/vector elements, while the superscripts represent the corresponding iteration cycles.

Within each sampling period, the iteration terminates once $\boldsymbol{\lambda}$ converged or the specified iteration upperlimit is exceeded. Note that no matrix inversion is required in the iterations, the computational complexity for each iteration cycle is moderate.

The respective computation time of the proposed CCS-PSC and cascaded CCS-PSC in dSPACE SCALEXIO real-time controller is shown in Table VII. Only the maximum required computation time of each method is recorded. For the proposed CCS-PSC, the iteration upperlimit is 20. As can be seen from the table, the maximum required computation time is only 2.6 μs, which is 1/6.38 times of that with the cascaded CCS-PSC. For cascaded CCS-PSC with long prediction horizon, inversion of matrices with high order is computational expensive. It can be concluded that with the proposed CCS-PSC, the computational complexity is relatively low.

B. Noise Immunity

In electrical drives noises commonly exist, including but not limited to speed and current measurement noises. For high bandwidth controller such as CCS-PSC, noise immunity is critical. Low noise immunity leads to excessive variation of inverter output voltages as well as high frequency current ripples. These high frequency current ripples pose challenges to the rotor shaft and the permanent magnet. Moreover, the resulting iron losses and copper losses deteriorate the overall system efficiency. Thus, the current THD should be relatively low in the presence of noises.

TABLE VIII
INFLUENCE OF k_u ON CURRENT THD (LOAD TORQUE: 4 NM)

k_u	Speed: 300 r/min	Speed: 2000 r/min
0	6.25%	5.55%
1e-4	3.68%	3.28%

In the proposed CCS-PSC, the weighting factor k_u is used to achieve low sensitivity to noises. With a nonzero k_u, noise related unnecessary variations of the output voltages are penalized. In consequence, the current THD can be improved. Table VIII shows the influence of k_u on current THD at low speed (300 r/min) and high speed (2000 r/min) operation. The load torque is 4 N $\cdot$ m. For k_u equal to 0, the current THD is relatively high. Increase k_u merely to 1e-4, current THD decreases significantly.

To better illustrate the influence of k_u, the acceleration process of the proposed CCS-PSC is revisited. With k_u equal to 0, the acceleration process is shown in Fig. 8. The motor accelerates from standstill to 2000 r/min, while the load torque is not actively applied. Compared with Fig. 3(b) ($k_u =$ 1e-4), the d-axis current deviates more from the horizontal axis during the acceleration. Moreover, ripples in d-axis current are relatively large. Since no penalization is posed on the variations of voltage, the d-axis voltage varies excessively due to the low signal-to-noise ratio in d-axis current. The consequence is the poorly controlled d-axis current, filled with high frequency ripples.

Based on the experimental results and theoretical analysis, a nonzero weighting factor k_u is suggested to achieve noise immunity.

C. Robustness Against Parameter Mismatches in Inertia

In practical applications, model uncertainties and parameter mismatches are often the case. To tackle this issue, incremental SPMSM model, which naturally includes integral actions is used in the proposed CCS-PSC. As shown in Section IV, no SSE in speed is observed.

Note that the system inertia is related to the mechanical part (e.g., control side motor, couplings as well as the load side motor), which cannot be extracted directly from the motor nameplates. Instead, the inertia is obtained through acceleration/deceleration tests. The calculation of the inertia is based on the mechanical model, which may be inaccurate. In addition, the nonlinear properties of the friction coefficient complicates the calculation.

Therefore, the robustness of the proposed CCS-PSC is investigated with parameter mismatches in inertia J, which is shown in Fig. 9. The motor accelerates from standstill to 500 r/min without actively applied load torque. For each acceleration, the parameter inertia in the prediction model differs from one another. As can be seen from the figure, the speed settling time varies. Nonetheless, the actual speed is able to track the

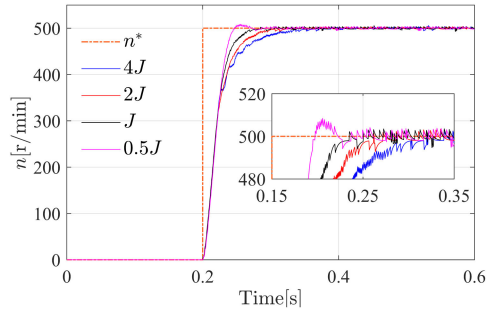

Fig. 9. [Experimental results:] Acceleration performance of the proposed CCS-PSC with parameter mismatches in inertia J.

reference accurately at steady-state. The result demonstrates that the proposed CCS-PSC is robust to a wide range varying J.

VI. Conclusion

In this article, a CCS–PSC strategy with short prediction horizon has been proposed to achieve balanced steady-state and dynamic performances. The optimization problem has been formulated as a QP. The current and voltage constraints have been reformulated and transformed into respective incremental voltage constraints, which facilitates the solving of the QP. Reduced-order incremental SPMSM model has been used, where the integral action is naturally embedded. In this way, SSE in the speed is eliminated. Comparative experiments have been implemented to evaluate the performance of the proposed CCS-PSC. As can be seen from the experimental results, low current THD is obtained, while high dynamic speed responses are maintained with the proposed CCS-PSC.

References

[1] J. Rodriguez *et al.*, "State of the art of finite control set model predictive control in power electronics," *IEEE Trans. Ind. Informat.*, vol. 9, no. 2, pp. 1003–1016, May 2013.

[2] S. Vazquez, J. Rodriguez, M. Rivera, L. G. Franquelo, and M. Norambuena, "Model predictive control for power converters and drives: Advances and trends," *IEEE Trans. Ind. Electron.*, vol. 64, no. 2, pp. 935–947, Feb. 2017.

[3] S. Kouro, P. Cortes, R. Vargas, U. Ammann, and J. Rodriguez, "Model predictive control—A simple and powerful method to control power converters," *IEEE Trans. Ind. Electron.*, vol. 56, no. 6, pp. 1826–1838, Jun. 2009.

[4] P. Cortes, M. P. Kazmierkowski, R. M. Kennel, D. E. Quevedo, and J. Rodriguez, "Predictive control in power electronics and drives," *IEEE Trans. Ind. Electron.*, vol. 55, no. 12, pp. 4312–4324, Dec. 2008.

[5] Y. Zhang, D. Xu, J. Liu, S. Gao, and W. Xu, "Performance improvement of model-predictive current control of permanent magnet synchronous motor drives," *IEEE Trans. Ind. Appl.*, vol. 53, no. 4, pp. 3683–3695, Jul./Aug. 2017.

[6] F. Wang, S. Li, X. Mei, W. Xie, J. Rodríguez, and R. M. Kennel, "Model-based predictive direct control strategies for electrical drives: An experimental evaluation of PTC and PCC methods," *IEEE Trans. Ind. Informat.*, vol. 11, no. 3, pp. 671–681, Jun. 2015.

[7] I. Gonzalez-Prieto, M. J. Duran, J. J. Aciego, C. Martin, and F. Barrero, "Model predictive control of six-phase induction motor drives using virtual voltage vectors," *IEEE Trans. Ind. Electron.*, vol. 65, no. 1, pp. 27–37, Jan. 2018.

[8] T. Geyer, G. Papafotiou, and M. Morari, "Model predictive direct torque control-Part I: Concept, algorithm, and analysis," *IEEE Trans. Ind. Electron.*, vol. 56, no. 6, pp. 1894–1905, Jun. 2009.

[9] C. A. Rojas, J. Rodriguez, F. Villarroel, J. R. Espinoza, C. A. Silva, and M. Trincado, "Predictive torque and flux control without weighting factors," *IEEE Trans. Ind. Electron.*, vol. 60, no. 2, pp. 681–690, Feb. 2013.

[10] J. Rodriguez, R. M. Kennel, J. R. Espinoza, M. Trincado, C. A. Silva, and C. A. Rojas, "High-performance control strategies for electrical drives: An experimental assessment," *IEEE Trans. Ind. Electron.*, vol. 59, no. 2, pp. 812–820, Feb. 2012.

[11] J. A. Riveros, F. Barrero, E. Levi, M. J. Durán, S. Toral, and M. Jones, "Variable-speed five-phase induction motor drive based on predictive torque control," *IEEE Trans. Ind. Electron.*, vol. 60, no. 8, pp. 2957–2968, Aug. 2013.

[12] H. Guzman, F. Barrero, and M. J. Duran, "IGBT-gating failure effect on a fault-tolerant predictive current-controlled five-phase induction motor drive," *IEEE Trans. Ind. Electron.*, vol. 62, no. 1, pp. 15–20, Jan. 2015.

[13] J. Wang, F. Wang, Z. Zhang, S. Li, and J. Rodríguez, "Design and implementation of disturbance compensation-based enhanced robust finite control set predictive torque control for induction motor systems," *IEEE Trans. Ind. Informat.*, vol. 13, no. 5, pp. 2645–2656, Oct. 2017.

[14] L. Yan, M. Dou, Z. Hua, H. Zhang, and J. Yang, "Robustness improvement of fcs-mptc for induction machine drives using disturbance feedforward compensation technique," *IEEE Trans. Power Electron.*, vol. 34, no. 3, pp. 2874–2886, Mar. 2019.

[15] M. Preindl and S. Bolognani, "Model predictive direct speed control with finite control set of PMSM drive systems," *IEEE Trans. Power Electron.*, vol. 28, no. 2, pp. 1007–1015, Feb. 2013.

[16] E. J. Fuentes, C. Silva, D. E. Quevedo, and E. I. Silva, "Predictive speed control of a synchronous permanent magnet motor," in *Proc. IEEE Int. Conf. Ind. Technol.*, 2009, pp. 1–6.

[17] X. Gao, M. Abdelrahem, C. M. Hackl, Z. Zhang, and R. Kennel, "Direct predictive speed control with a sliding manifold term for PMSM drives," *IEEE Trans. Emerg. Sel. Topics Power Electron.*, vol. 8, no. 2, pp. 1258–1267, Jun. 2020.

[18] J. Rodríguez, M. A. Pérez, H. Young, and H. Abu-Rub, "Model predictive speed control of electrical machines," in *Proc. Power Electron. Renewable Energy Syst., Transp. Ind. Appl.*, 2014, pp. 608–629.

[19] P. Kakosimos and H. Abu-Rub, "Predictive speed control with short prediction horizon for permanent magnet synchronous motor drives," *IEEE Trans. Power Electron.*, vol. 33, no. 3, pp. 2740–2750, Mar. 2018.

[20] A. Darba, F. De Belie, P. D'haese, and J. A. Melkebeek, "Improved dynamic behavior in BLDC drives using model predictive speed and current control," *IEEE Trans. Ind. Electron.*, vol. 63, no. 2, pp. 728–740, Feb. 2016.

[21] X. Zhang and Y. He, "Direct voltage-selection based model predictive direct speed control for PMSM drives without weighting factor," *IEEE Trans. Power Electron.*, vol. 34, no. 8, pp. 7838–7851, Aug. 2019.

[22] X. Zhang, Y. Cheng, Z. Zhao, and Y. He, "Robust model predictive direct speed control for SPMSM drives based on full parameter disturbances and load observer," *IEEE Trans. Power Electron.*, vol. 35, no. 8, pp. 8361–8373, Aug. 2020.

[23] P. G. Carlet, F. Toso, A. Favato, and S. Bolognani, "A speed and current cascade continuous control set model predictive control architecture for synchronous motor drives," in *Proc. IEEE Energy Convers. Congr. Expo.*, 2019, pp. 5682–5688.

[24] S. Wendel, B. Haucke-Korber, A. Dietz, and R. Kennel, "Cascaded continuous and finite model predictive speed control for electrical drives," in *Proc. 20th Eur. Conf. Power Electron. Appl.*, 2018, pp. P.1–P.10.

[25] N. Jabbour and C. Mademlis, "Online parameters estimation and autotuning of a discrete-time model predictive speed controller for induction motor drives," *IEEE Trans. Power Electron.*, vol. 34, no. 2, pp. 1548–1559, Feb. 2019.

[26] L. Wang, S. Chai, D. Yoo, L. Gan, and K. Ng, "Discrete-time model predictive control (DMPC) of electrical drives and power converter," in *Proc. PID Predictive Control Elect. Drives Power Converters Using MATLAB/Simulink*, 2015, pp. 265–284.

[27] H. T. Nguyen and J. Jung, "Finite control set model predictive control to guarantee stability and robustness for surface-mounted PM synchronous motors," *IEEE Trans. Ind. Electron.*, vol. 65, no. 11, pp. 8510–8519, Nov. 2018.

[28] J. Jung, V. Q. Leu, T. D. Do, E. Kim, and H. H. Choi, "Adaptive PID speed control design for permanent magnet synchronous motor drives," *IEEE Trans. Power Electron.*, vol. 30, no. 2, pp. 900–908, Feb. 2015.

[29] T. Geyer, *Model Predictive Control of High Power Converters and Industrial Drives*. Hoboken, NJ, USA: Wiley, 2016.

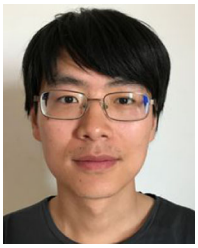

Xicai Liu (Student Member, IEEE) received the double M.S. degree in control engineering from Tongji University, Shanghai, China and Technische Universitaet Muenchen, Munich, Germany in 2013.

Since 2014, he was been with Huazhong University of Science and Technology (HUST), Wuhan, China, where he was awarded the Ph.D. degree in electrical engineering. His major research interests include predictive control of electrical drives and power electronics.

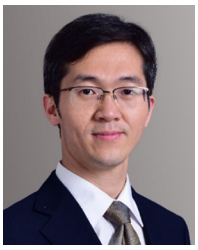

Jin Wang (Member, IEEE) received the B.S., M.S., and Ph.D. degrees in electrical engineering from the Huazhong University of Science and Technology, Wuhan, China, in 2002, 2005, and 2010, respectively.

From 2010 to 2013, he was a Postdoctoral Fellow with Huazhong University of Science and Technology. He is currently an Associate Professor with the Huazhong University of Science and Technology, Wuhan, China. His research interests include design and control of permanent magnet brushless machines.

Xiaonan Gao (Member, IEEE) was born in Liaoning, China, in 1990. He received the B.S. and M.S. degrees in electrical engineering from the Dalian University of Technology, Dalian, China, in 2013 and 2016, respectively. He is currently working toward the Ph.D. degree in predictive control of modular multilevel converter with the Institute for Electrical Drive Systems and Power Electronics, Technical University of Munich, Germany.

His research interests include power electronics and electrical drives, predictive control, and multilevel converters.

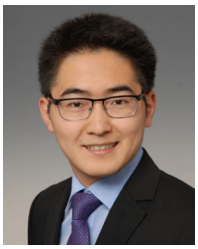

Wei Tian (Student Member, IEEE) was born in Taizhou, Jiangsu, China, in 1989. He received the B.Eng. degree in electrical engineering and automation from Central South University, Changsha, China, in 2012, and the M.Sc. degree in electrical power engineering from RWTH Aachen University, Aachen, Germany, in 2015. Since 2016, he has been working toward the Ph.D. degree in predictive control of modular multilevel converter with the Chair of Electrical Drive Systems and Power Electronics, Technical University of Munich, Munich, Germany.

His research interests include power electronics and electrical drives, model predictive control, and modular multilevel converter.

Libing Zhou (Member, IEEE) received the B.S., M.S., and Ph.D. degrees from Huazhong University of Science and Technology, Wuhan, China, in 1982, 1985, and 1993, respectively, all in electrical engineering.

He is currently a Professor with Huazhong University of Science and Technology, Wuhan, China. His research interests include electromagnetic design, operation analysis, and drives of ac machines.

Jose Rodriguez (Life Fellow, IEEE) received the Engineer degree in electrical engineering from the Universidad Tecnica Federico Santa Maria, in Valparaiso, Chile, in 1977, and the Dr.-Ing. degree in electrical engineering from the University of Erlangen, Erlangen, Germany, in 1985.

Since 1977, he has been with the Department of Electronics Engineering, Universidad Tecnica Federico Santa Maria, where he was full Professor and President. Since 2015, he was the President and since 2019 he is Full Professor with Universidad Andres Bello in Santiago, Chile. He has coauthored two books, several book chapters, and more than 400 journal and conference papers. His main research interests include multilevel inverters, new converter topologies, control of power converters, and adjustable-speed drives.

Dr. Rodriguez was a recipient of number of best paper awards from IEEE journals. He is member of the Chilean Academy of Engineering. In 2014, he received the National Award of Applied Sciences and Technology from the government of Chile. In 2015, he received the Eugene Mittelmann Award from the IEEE Industrial Electronics Society. In 2014 to 2020, he has been included in the list of Highly Cited Researchers published by Web of Science.

Ralph Kennel (Senior Member, IEEE) was born in Kaiserslautern, Germany, in 1955. He received the Diploma and Dr. Ing. (Ph.D.) degrees in electrical engineering from the University of Kaiserslautern, Kaiserslautern, Germany, in 1979 and 1984, respectively.

From 1983 to 1999, he worked on several positions with Robert BOSCH GmbH (Germany). Until 1997, he was responsible for the development of servo drives. From 1994 to 1999, he was a Visiting Professor with the University of Newcastle-upon-Tyne, Newcastle-upon-Tyne, U.K. From 1999 to 2008, he was a Professor of electrical machines and drives with Wuppertal University, Wuppertal, Germany. Since 2008, he has been a Professor of electrical drive systems and power electronics with Technical University of Munich, Munich, Germany. His current main interests include renewable energy systems, sensorless control of ac drives, predictive control of power electronics, and hardware-in-the-loop systems.

Prof. Kennel is a Fellow of the IEE and a Chartered Engineer in the U.K. within IEEE, he is a Treasurer of the Germany Section as well as ECCE Global Partnership Chair of the Power Electronics society. He is an Associate Editor for the IEEE TRANSACTIONS ON POWER ELECTRONICS.